Supplementary Information for "Acoustic Bilayer Gradient Metasurfaces for Perfect and Asymmetric Beam Splitting"

Jiaqi Quan[1], Baoyin Sun[1], Yangyang Fu[2*], Lei Gao[1, 3] and Yadong Xu[1*]

[1]*Institute of Theoretical and Applied Physics, School of Physical Science and Technology, Soochow University, Suzhou 215006, China*

[2]*College of Physics, Nanjing University of Aeronautics and Astronautics & Key Laboratory of Aerospace Information Materials and Physics (NUAA), MIIT, Nanjing, 211106, China*

[3]*School of Optical and Electronic Information, Suzhou City University, Suzhou 215104, China*

Supplementary Note 1. Diffraction of single AGM-1 and AGM-2 via different incidence angles.

Supplementary Note 2. The artificial microstructure design for the AGMs.

Supplementary Note 3. Simulation and experimental observation of the diffraction effect of single-layer AGM-1 and AGM-2.

Supplementary Note 4. The performance of our model via different working frequencies and incidence angles.

Supplementary Note 5. The influence of the acoustic bilayer metasurfaces under different horizontal slips.

Supplementary Note 1. Diffraction of single AGM-1 and AGM-2 via different incidence angles.

Considering the influence of different incidence angles on the AGMs, in Supplementary Figure 1(a), we calculated the diffraction efficiency of AGM-1 with different k_x, where the phase gradient along the surface is $\xi_1 = \sqrt{2}k_0$, and we find that the transmission efficiency is zero from k_x/k_0=-0.41 to 0.41, which means that in this interval of AGM-1, the evanescent waves will occur along the structure. But for AGM-2, it is obvious that two diffraction channels of +1 and -1 are open, and the transmission around 0.5. The key concept involves the evanescent field. Hence, auxiliary generation of the evanescent fields of AGM-1 plays a key role in the bilayer metasurfaces structure, and the near-field efficiencies of T_1, T_{-1} and R_0 are shown in Supplementary Figure 1(c), where schematic diagram of the T_1, T_{-1} and R_0 are shown in

* yyfu@nuaa.edu.cn
* ydxu@suda.edu.cn

Supplementary Figure 1(d).

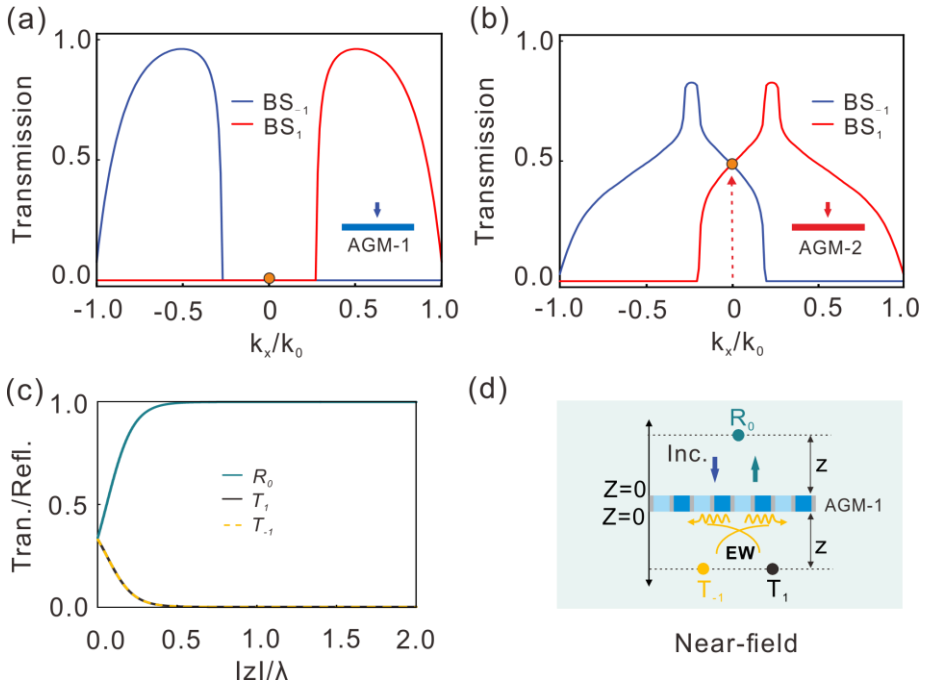

Figure S1. Transmission efficiency of BS-1 and BS-2 via different incidence angles (i.e., k_x) for (a) AGM-1 and (b) AGM-2. (c) Near field transmission/reflection efficiency of AGM-1, and (d) its schematic diagram.

Supplementary Note 2. The artificial microstructure design for the AGMs.

In order to design acoustic bilayer metasurfaces, a coiling-up structure is proposed to obtain coded phase elements of "0" and "π" (see Supplementary Figure 2(a)). The working frequency is selected as 3430 Hz (λ=10 cm), and the coiling-up subcell consists of multiple building blocks and has identical wall thickness t = 0.2 cm, height $h = 0.5\lambda$, width $w = 0.35\lambda$ and $a = w - 2t$. The phase shift trend of one cycle can be calculated by changing the length b (see the black curve in Supplementary Figure 2(b)), and the corresponding transmission is represented by the blue curve. Two binary unit cells with "0" and "π" phases are selected and marked with red dots, where $b = 0$ and $b = 0.45a$ and the average transmission of these unit cells is beyond 99%. To be more intuitive, the detailed parameters are placed in Supplementary Figure 2(c). Based on these two designed parameters in Supplementary Figure 2(c), we can obtain the expected AGMs structure. 3D printing enables direct fabrication of AGM-1 and AGM-2.

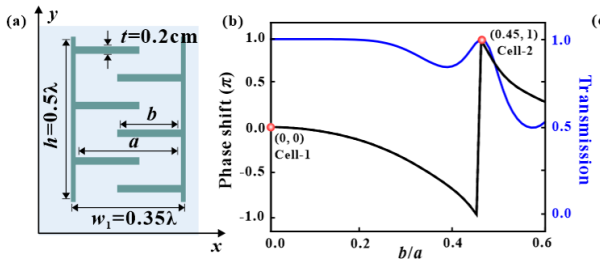

Unit cells	Cell-1	Cell-2
Ratio(b/a)	0.0	0.45
Phase	0	π
Transmission	0.99	0.99

Figure S2. (a) Schematic illustration of the coiling-up structure, the (b) phase shift and transmission with a function of b/a. (c) Selected coded phase elements sizes of "0" and "π".

Supplementary Note 3. Simulation and experimental observation of the diffraction effect of single-layer AGM-1 and AGM-2.

Here, we calculated the modulation behavior of single-layer AGMs in both simulation and experiment. Due to $\xi_1 > k_0$ in AGM-1, the acoustic wave incidence on AGM-1 introduces zero diffraction orders, as shown in Supplementary Figure 3(a), the structural surface appeared evanescent waves and most of the energy is blocked along the surface by AGM-1. To fully demonstrate this phenomenon, we measured the acoustic amplitude distribution at the position of 1 cm (Supplementary Figure 3(a) yellow dotted line location) from the surface of AGM-1 in Supplementary Figure 3(b), the measured range is from -45 cm to 45 cm and the step size is 1 cm. The experimental results match well with the simulation results, and the largest amplitude is mainly concentrated in the center of AGM-1, which indicates that the evanescent waves are excited under the acoustic wave incidence of AGM-1. For AGM-2 with $\xi_2 < k_0$ in Supplementary Figure 3(c), we can clearly find that the outgoing acoustic beam split into two waves, consistent with our theoretical analysis, which the beam splitting effect is introduced due to the structural diffraction orders of n = ±1. In order to verify the beam splitting effect, we measured the amplitude field distribution at a location 60 cm from the sample of AGM-2, as shown in the yellow dotted line in Supplementary Figure 3(c), the measured results are shown in the blue dotted line in Supplementary Figure 3(d), where the energy is mainly concentrated on the two sides and the middle is smaller.

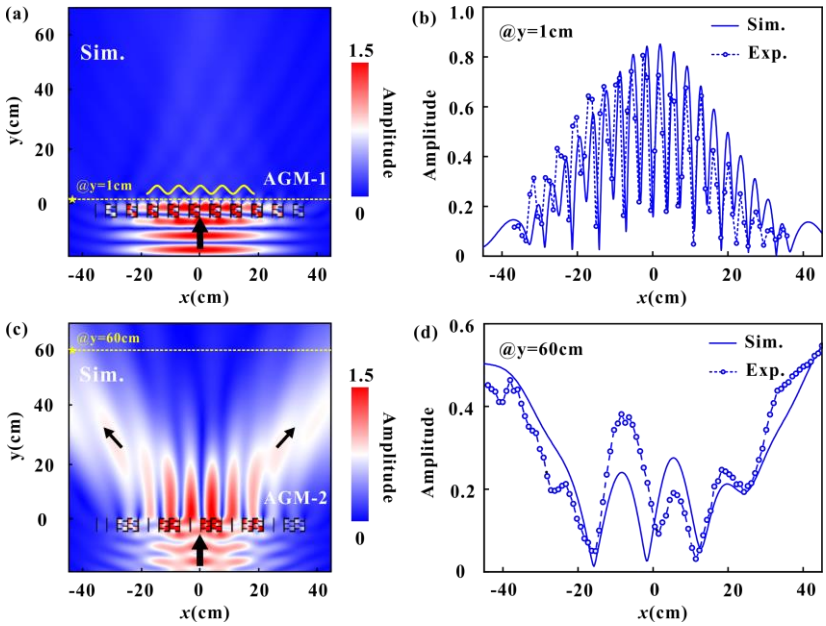

Figure S3. The simulated amplitude field of (a) AMG-1 and (c) AMG-2, and the measured acoustic amplitude intensity distribution at the positions of (b) y = 1 cm and (d) y = 60 cm.

Supplementary Note 4. The performance of our model via different working frequencies and incidence angles.

To quantitatively reveal the performance of the symmetric/asymmetric transmission effect, the contrast ratio ($|\eta|$) of the transmission energy is defined as $|\eta| = \left|T_{Negative} - T_{Positive}\right| / \left(T_{Negative} + T_{Positive}\right)$, where $T_{Positive}$ and $T_{Negative}$ are transmission for positive incidence and negative incidence, respectively. The transmission energy in both cases are measured at the distance of 2λ away from the sample. Supplementary Figure 4(a) shows the relationship between the contrast ratio and the different frequencies. The considered frequency range is operated near the central frequency of 3430 Hz, i.e., from 3.0 kHz to 3.8 kHz. Excellently, the contrast ratio of the asymmetric transmission in experiments can maintain a good performance ($|\eta| \geq 0.8$) from 3.24 to 3.54 kHz and thus has a bandwidth of about 7.8% of the central frequency, which slightly deviates from that of 6.8% in the simulation (see the blue curves in Supplementary Figure 4(a)). For the case of d=0, as shown by the red curves in Supplementary Figure 4(a), we can clearly find that the contrast ratios are below 20% in both simulations and experiments. Although the proposed dual-layer metasurfaces are made of simple acoustic structures, the asymmetric transmission performance can maintain a certain band of frequencies, which is useful in practical applications. In addition, we also find that asymmetric transmission can work not only at normal

incidence but also at oblique incidence. As shown in Supplementary Figure 4(b). We changed the incidence angles but keep the operating frequency at 3430 Hz. The same as the previous experimental environment, but the incidence angle needs to be changed. We can observe that the asymmetric transmission (blue line) contrast ratio is greater than 60% for both shaded regions (0° to 17° and 36° to 68°), which formed due to the segmentation of the critical angle (arcsin (λ/p_1 - 1)≈24.5°) in the system. For d=0, the system has a symmetrical diffraction channel so that it has high efficiency beam splitting effect for both sides incidence, and the contrast ratio is below 20%, as shown by the red line in Supplementary Figure 4(b). The results show that our acoustic bilayer metasurfaces have good robustness to both the working frequencies and the incidence angles.

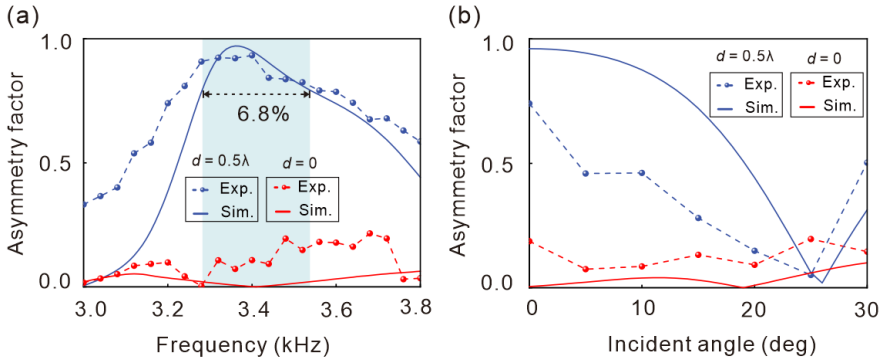

Figure S4. (a) Frequency response of extremely asymmetric beam splitting in acoustic bilayer metasurfaces. (b) Contrast ratio of the transmission energy versus the different incidence angles. The blue (red) curves represent the case of air-gap d=0.5λ (d=0) transmission, and the solid and dotted curves represent the simulated and experimental results, respectively.

Supplementary Note 5. The influence of the acoustic bilayer metasurfaces under different horizontal slips.

Here, we consider the acoustic incidences on both sides of the system under d=0.5λ, with the horizontal slip L changes, we find that the total transmission efficiency still maintains a high level, which means that in this case the horizontal slip is nonfunctional, where the blue line is the negative incidence and the red line is the positive incidence. Typically, when L=p/4, the transmission efficiency is lowest for the negative incidence, and the transmission efficiencies are about 98.97% and 0.19% at L=p/4 for the positive and negative incidences, respectively. To intuitively observe, we show the amplitude of both sides incident on the bilayer metasurfaces, and the asymmetric beam splitting effect can still be maintained.

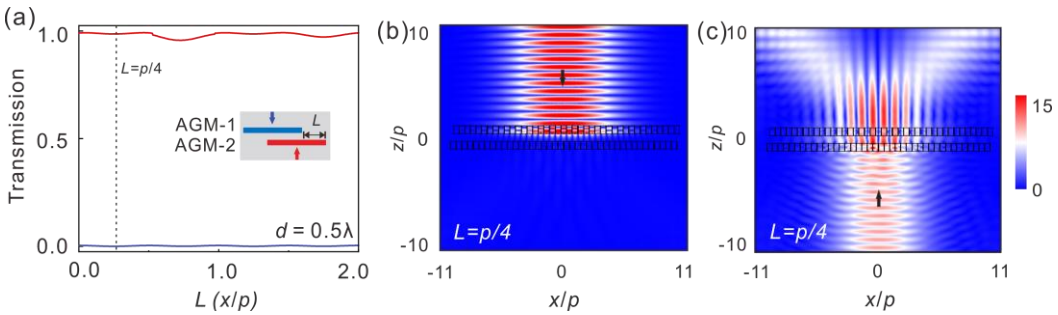

Figure S5. (a) The influence of transmission efficiency via different horizontal slips for the cases of d=0.5λ, (b) and (c) are the amplitude distributions at the horizontal slip L=p/4 for the cases of negative incidence and positive incidence, respectively.